ACS NANO
Cite This: ACS Nano 2018, 12, 644−650
www.acsnano.org

ARTICLE

Highly Enhanced Third-Harmonic Generation in 2D Perovskites at Excitonic Resonances

Ibrahim Abdelwahab,[†,‡,§] Gustavo Grinblat,[‡] Kai Leng,[†] Yi Li,[‡] Xiao Chi,[∥] Andrivo Rusydi,[∥] Stefan A. Maier,[*,‡,⊥] and Kian Ping Loh[*,†]

[†]Centre for Advanced 2D Materials (CA2DM) and Department of Chemistry, National University of Singapore, Singapore 117546
[‡]The Blackett Laboratory, Department of Physics, Imperial College London, London SW7 2AZ, United Kingdom
[§]NUS Graduate School for Integrative Sciences and Engineering, National University of Singapore, Singapore 117456
[∥]Department of Physics and Singapore Synchrotron Light Source, National University of Singapore, Singapore 119077
[⊥]Fakultät für Physik, Ludwigs-Maximilians-Universität München, 80799 München, Germany

Supporting Information

ABSTRACT: **Two-dimensional hybrid organic−inorganic Ruddlesden−Popper perovskites (RPPs) have attracted considerable attention due to their rich photonic and optoelectronic properties. The natural multi-quantum-well structure of 2D RPPs has been predicted to exhibit a large third-order nonlinearity. However, nonlinear optical studies on 2D RPPs have previously been conducted only on bulk polycrystalline samples, in which only weak third-harmonic generation (THG) has been observed. Here, we perform parametric nonlinear optical characterization of 2D perovskite nanosheets mechanically exfoliated from four different lead halide RPP single crystals, from which we observe ultrastrong THG with a maximum effective third-order susceptibility ($\chi^{(3)}$) of 1.12 × 10^{-17} m^2 V^{-2}. A maximum conversion efficiency of 0.006% is attained, which is more than 5 orders of magnitude higher than previously reported values for 2D materials. The THG emission is resonantly enhanced at the excitonic band gap energy of the 2D RPP crystals and can be tuned from violet to red by selecting the RPP homologue with the requisite resonance. Due to signal depletion effects and phase-matching conditions, the strongest nonlinear response is achieved for thicknesses less than 100 nm.**

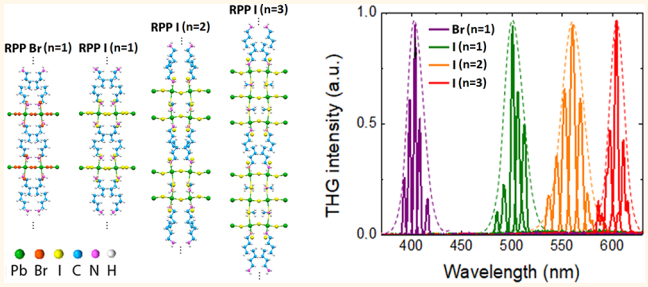

KEYWORDS: *2D Ruddlesden−Popper perovskites, third-harmonic generation, multiquantum wells, excitonic resonances, phase matching*

Search for materials that can efficiently convert low-frequency light photons into high-frequency light photons through nonlinear optical (NLO) processes[1] has been a subject of extensive studies for many years. Among various NLO processes, second-harmonic generation (SHG) and third-harmonic generation (THG) have been widely utilized to convert near- and mid-IR light into UV/visible light, which can be applied in a wide range of applications such as nonlinear correlation spectroscopy,[2] photovoltaics,[3] coherent ultraviolet light generation,[4] bioimaging,[5] and drug delivery.[6] Recently, 2D materials including graphene,[7,8] hexagonal boron nitride (h-BN),[9] black phosphorus (BP),[10,11] MoS_2,[12−14] $MoSe_2$,[15,16] WS_2,[17] WSe_2,[18] GaSe,[19] and InSe[20] have shown potential as ultrathin NLO materials with large nonlinearities. It has also been found that thickness tuning,[11] electrical control,[21] and resonant excitonic excitation[10,13,22,23] can significantly enhance the nonlinear optical response of 2D optical media. However, frequency conversion at the nanoscale turns out to be very challenging due to the difficulty in achieving high nonlinear conversion efficiency and subwavelength phase control.[24] To improve the efficiency of light−matter interactions, nanostructured optical components based on plasmonic and dielectric nanoantennas,[25−27] metasurfaces,[28−30] and multi-quantum-well (MQW) semiconductor media[31,32] have been introduced to enhance optical nonlinearities at subwavelength volumes.

The 2D hybrid organic−inorganic perovskites (HOIPs) have recently emerged as a promising class of materials due to their outstanding optoelectronic properties.[33−35] HOIPs have a natural MQW structure that is based on an inorganic semiconductor layer sandwiched by organic dielectric layers, leading to strong excitonic effects due to quantum confinement.[36] The 2D hybrid lead halide Ruddlesden−Popper

Received: October 30, 2017
Accepted: December 20, 2017
Published: December 20, 2017

DOI: 10.1021/acsnano.7b07698
ACS Nano 2018, 12, 644−650

perovskites (RPPs)[37] with the general formula $(RNH_3)_2(CH_3NH_3)_{n-1}Pb_nX_{3n+1}$ (n = 1, 2, 3, 4,...), where R is an alkyl or aromatic moiety and X is a halogen, are typical examples of 2D HOIPs. Increasing n in the formula allows more inorganic perovskite layers to be inserted between the organic chains, and at the extreme where $n \rightarrow \infty$, the structure transits into a 3D perovskite. Similar to most van der Waals bonded layered materials, the partially interdigitated organic layers in 2D RPPs can be spliced apart by a mechanical force or intercalation, hence presenting the interesting prospect of studying thickness-dependent phenomena.

Excitons in 2D RPPs possess high exciton binding energies and are delocalized within the inorganic perovskite layer (Wannier-like behavior).[38,39] In the perpendicular direction, however, excitons remain localized (Frenkel-like behavior), leading to high oscillator strengths that facilitate the generation of high exciton densities. The large populations of thermally stable and delocalized excitons in 2D RPP quantum wells can interact strongly enough to make them deviate from ideal bosons (*i.e.*, harmonic oscillators). Thus, strong third-order optical nonlinearities can be expected in 2D RPPs under resonant exciton excitation.[40,41] However, studies on the optical properties of 2D perovskites have mainly been carried out on polycrystalline films and powders.[37−39,42,43] The presence of grain boundaries and defect states in these bulk polycrystalline samples limits the coherent length of the 2D excitons, and therefore, weak THG has been reported for 2D RPPs.[37,43]

In this article, we study large-size 2D RPP single crystals of $(C_4H_9NH_3)_2PbBr_4$ (n = 1), $(C_4H_9NH_3)_2PbI_4$ (n = 1), $(C_4H_9NH_3)_2(CH_3NH_3)Pb_2I_7$ (n = 2), and $(C_4H_9NH_3)_2(CH_3NH_3)_2Pb_3I_{10}$ (n = 3), which present excitonic emissions in the 400 to 650 nm wavelength range. Exfoliating these single crystals down to monolayers using micromechanical cleavage followed by h-BN encapsulation enables us to investigate their optical nonlinearities as a function of thickness without risk of sample degradation. We discover that 2D RPP nanosheets exhibit a very large THG signal that varies strongly with the thickness and the excitation wavelength due to signal depletion, phase-matching conditions, and excitonic effects. In addition, due to their centrosymmetric orthorhombic crystal structure, our 2D RPP crystals show negligible second-order nonlinearities, in contrast to the defect-related SHG reported previously for the polycrystalline crystals.[37]

RESULTS AND DISCUSSION

Four different high-quality, millimeter-sized homologous 2D hybrid lead iodide/bromide RPP crystals (n = 1, 2, 3) were prepared through a temperature-lowering crystallization method[37] (for lead iodide RPPs) or an antisolvent vapor diffusion method[44] (for lead bromide RPPs) (see Methods section for fabrication specifics and section S1 in the Supporting Information (SI) for photographs of the RPP single crystals). Figure 1 schematizes the various obtained configurations, $(C_4H_9NH_3)_2PbBr_4$ (n = 1), $(C_4H_9NH_3)_2PbI_4$ (n = 1), $(C_4H_9NH_3)_2(CH_3NH_3)Pb_2I_7$ (n = 2), and $(C_4H_9NH_3)_2(CH_3NH_3)_2Pb_3I_{10}$ (n = 3), hereafter denoted as $Br_{n=1}$, $I_{n=1}$, $I_{n=2}$, and $I_{n=3}$, respectively. In all cases, the as-grown large-sized crystals showed single phase purity, as evidenced by X-ray diffraction (XRD) analysis performed on powder ground from a large batch of crystals (refer to section S2 in the SI for XRD data).

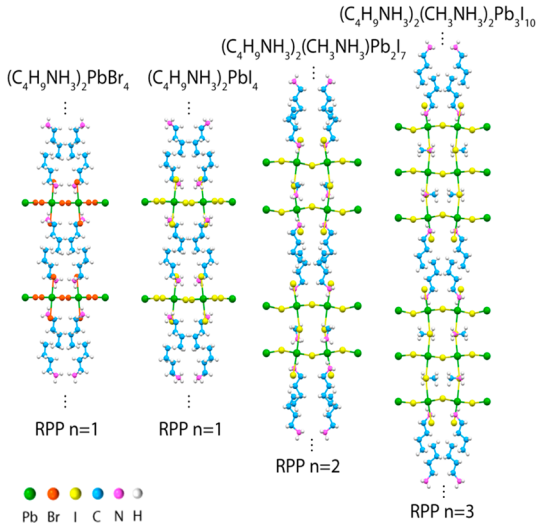

Figure 1. Diagram showing a side view of the bilayer crystal configurations corresponding to the different 2D RPP crystals.

The linear optical properties of the various grown crystals were studied by spectroscopic ellipsometry (SE) and photoluminescence (PL) measurements (see Methods section for optical characterization details). Figure 2a,b shows the real (ε_1) and imaginary (ε_2) components of the dielectric function, $\varepsilon = \varepsilon_1 + i\varepsilon_2$, as determined through SE. Due to Miller's rule,[1] a higher ε_1 implies a larger third-order nonlinear response, and therefore, based on this only, $I_{n=2}$ would provide the best THG performance when considering pump wavelengths in the near-infrared. ε_2, on the other hand, describes absorption losses. In Figure 2b, the different peaks, which correspond to band gap absorption, are found to shift to longer wavelengths following the sequence $Br_{n=1} \rightarrow I_{n=1} \rightarrow I_{n=2} \rightarrow I_{n=3}$, covering frequencies from violet to red. Figure 2c exhibits the PL spectra registered for the n = 1 to 3 homologues, which are dominated by excitonic emissions. A shift in emission wavelength reflects band gap narrowing with a higher n number, following the trends of ε_2.

From the energy difference between the electronic band gap and the optical band gap, we can calculate the exciton binding energies for the different homologues (refer to section S3 in the SI for calculation details), which are determined to be 553, 375, 264, and 204 meV for $Br_{n=1}$, $I_{n=1}$, $I_{n=2}$, and $I_{n=3}$, respectively. These values are significantly larger than corresponding values for 3D hybrid lead halide perovskites (76 meV for $CH_3NH_3PbBr_3$ and 50 meV for $CH_3NH_3PbI_3$)[45] and 2D perovskites (480, 80, 50, and 20 meV for $Br_{n=1}$, $I_{n=1}$, $I_{n=2}$, and $I_{n=3}$, respectively)[37,46] reported previously. Hence, the confined 2D RPP excitons are stable against thermal dissociation at room temperature ($k_BT \sim 26$ meV). Next, we investigate if these excitonic effects can resonantly enhance the THG response.

Following bulk characterization, the different crystals were exfoliated into thin flakes and transferred onto commercial Si/SiO_2 substrates for thickness-dependent optical analysis. The exfoliation and dry transfer processes were carried out in a controlled argon environment to avoid degradation in air. Before exposing the samples to normal atmospheric conditions, they were covered with a hexagonal boron nitride (h-BN) thin layer (<10 nm) to prevent direct contact with air. We found that the exfoliated flakes show narrow line width PL peaks with small Stokes shifts of 1−12 nm (see section S4 in the SI), as

DOI: 10.1021/acsnano.7b07698
ACS Nano 2018, 12, 644−650

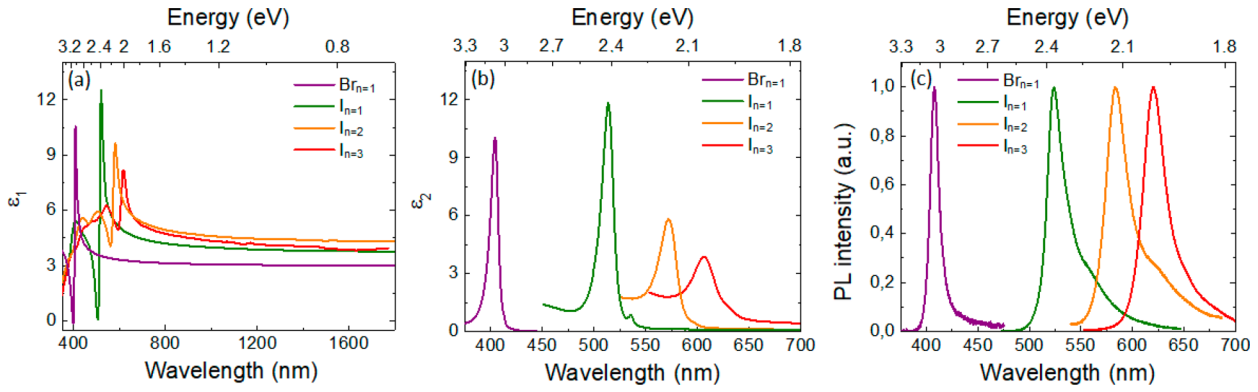

Figure 2. Real (a) and imaginary (b) components of the dielectric function ε for the four studied 2D RPP crystals and corresponding PL spectra (c). Excitation wavelengths employed for (c) are 325 nm ($Br_{n=1}$), 473 nm ($I_{n=1}$), and 532 nm ($I_{n=2,3}$).

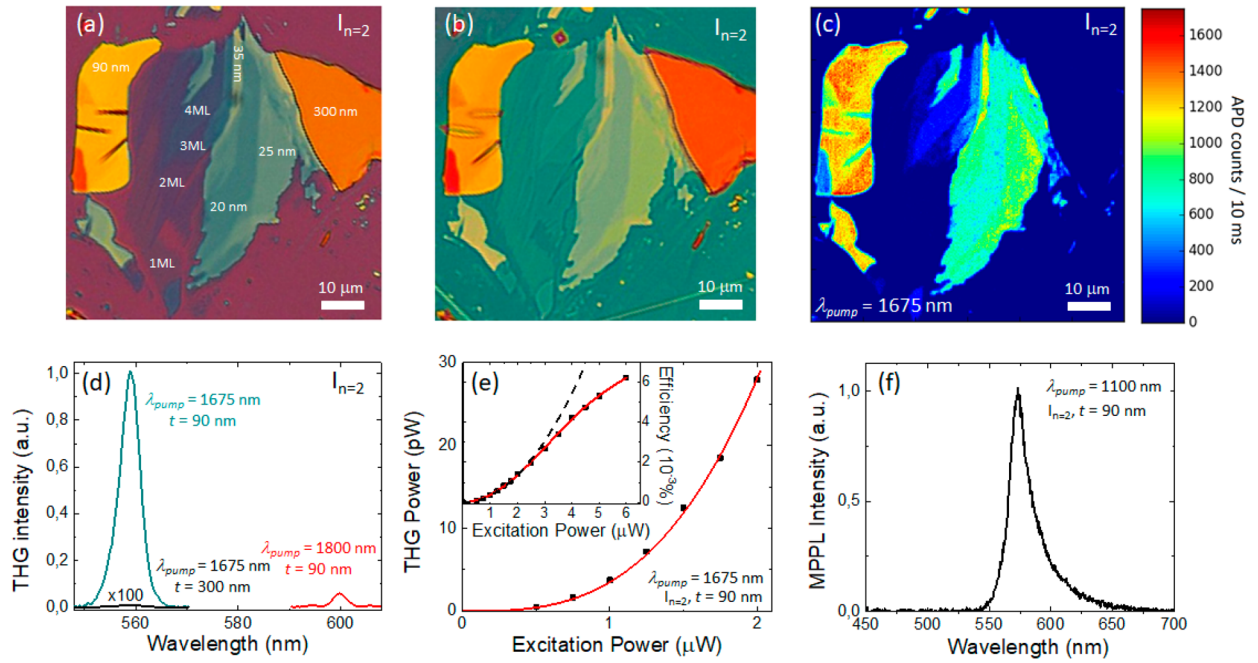

Figure 3. Optical image of $I_{n=2}$ flakes on Si/SiO_2 substrate before (a) and after (b) encapsulation with h-BN. The values in (a) denote corresponding thickness values (ML stands for monolayer). (c) THG image of the sample in (b) at λ_{pump} = 1675 nm. The acronym APD in the color scale stands for avalanche photodiode. (d) Corresponding THG spectra for selected excitation wavelengths and thicknesses labeled in the graph. (e) Excitation power dependence of the THG signal at λ_{pump} = 1675 nm for t = 90 nm. The line in the plot is fitted considering cubic dependence with the pump power. The inset shows the computed THG efficiency, η_{THG}, for a wider range of excitation powers (η_{THG} = THG power/pump power ∝ (pump power)^2). The red solid line connecting the experimental dots is found to deviate from a quadratic behavior (black dashed line) for pump powers larger than 2 μW. (f) Acquired spectrum at λ_{pump} = 1100 nm for t = 90 nm showing multiphoton absorption PL emission.

does the bulk, demonstrating that the exfoliation process does not diminish the quality of the crystals. We also notice that the PL peak position slightly blue shifts as the flake thickness decreases, probably due to in-plane crystal lattice expansion.[47] Figure 3a shows an optical image of obtained $I_{n=2}$ flakes as a representative example. As highlighted in the figure, the thickness (t) of the flakes varies from 2 nm (*i.e.*, 1 monolayer ≡ 1 ML) to 300 nm. Figure 3b shows the same area region as in Figure 3a after h-BN encapsulation, where a slight change in the color of the flakes can be perceived, together with a greenish surrounding introduced by the added h-BN layer. It is important to note that no degradation in the optical properties of the h-BN covered samples was observed throughout a period of several months, due to the effective encapsulation by h-BN (refer to SI section S5 for time stability data).

To analyze third-order nonlinear characteristics of the $I_{n=2}$ sample shown in Figure 3b, we studied its THG response when exciting at λ_{pump} = 1675 nm, so that the THG emission wavelength is resonant with the exciton energy (refer to Methods for nonlinear optical characterization details). Figure 3c shows a THG image of the sample registered at $\lambda = \lambda_{pump}/3$ = 558 nm, where a high contrast with respect to the h-BN background can be appreciated. Interestingly, it is observed that it is neither the thickest nor the thinnest layer that generates the largest nonlinear response, as the THG signal from the t = 300 nm and t = 1 monolayer regions is essentially negligible. The maximum THG signal occurs for intermediate t values, such as t = 90 nm. The corresponding nonlinear spectra of the sample in Figure 3b are presented in Figure 3d for selected conditions. In particular, at λ_{pump} = 1675 nm, it is observed that

DOI: 10.1021/acsnano.7b07698
ACS Nano 2018, 12, 644−650

the THG signal is 4 orders of magnitude lower for t = 300 nm compared to t = 90 nm. In addition, it is found that the high emission intensity registered for the t = 90 nm flake reduces significantly when the excitation wavelength is detuned so that the THG wavelength occurs at 600 nm, just outside the excitonic absorption peak region (see Figure 2b). These results indicate that there is a strong photon−exciton coupling in 2D RPPs that enhances the third-order nonlinear signal at resonant exciton excitation; but, at the same time, thickness-associated absorption and phase-matching effects prevent the thickest flakes from being the most efficient.[11]

The excitation power dependence of the nonlinear signal in the 0−2 μW (average) pump power range (0−110 W peak power range), as shown in Figure 3e for t = 90 nm at λ_{pump} = 1675 nm, reveals the expected cubic behavior characteristic of THG, as evidenced by the third-order polynomial fit (solid line). However, as shown in the inset of Figure 3e, the THG efficiency, calculated as the ratio between THG and excitation powers, starts to saturate above 2 μW. This saturation effect can be ascribed to heating effects, which can cause exciton dissociation and change optical characteristics of the material. Up to the maximum laser power used, no hysteresis of the THG signal as a function of pump power was observed, suggesting that the sample was not damaged. Remarkably, a maximum THG conversion efficiency of 0.006% is attained for $I_{n=2}$ RPP crystals, which is more than 5 orders of magnitude higher than values reported for 2D materials[11,14] and comparable to the highest THG efficiency reported using hybrid metal/dielectric nanoantennas.[48] Regarding SHG, there has been considerable debate over the crystal symmetry of butylammonium 2D RPPs, where nonpolar (centrosymmetric) and polar (noncentrosymmetric) assignments of their crystal structure have been reported.[37] In our case, when the pump wavelength is lowered to λ_{pump} = 1100 nm so as to induce resonant SHG at 550 nm, no SHG signal is observed, as shown in Figure 3f. Indeed, only multiphoton absorption PL (MPPL) is detected in the visible range (see Figure 2c for comparison with linear PL results (refer to the SI section S6 for additional MPPL experimental data). This finding contrasts with previous studies where strong SHG signal was measured due to the presence of defects that break the centrosymmetry of the crystals, and suggests that high-quality butylammonium 2D RPPs crystallize in centrosymmetric orthorhombic *Pcab* (n = 1), *Ccmm* (n = 2), and *Acam* (n = 3) space groups at room temperature.[37]

The results for the n = 1 to 3 RPP flakes are shown in Figure 4 (optical images of the samples can be found in section S7 in the SI). Figure 4a exhibits the THG spectra recorded for each type of crystal ($Br_{n=1}$, $I_{n=1}$, $I_{n=2}$, $I_{n=3}$) when varying the pump wavelength. Notably, in all cases, the THG signal is strongly enhanced when it is in resonance with the exciton absorption energy. This resonant behavior in the third-order nonlinear response can be understood from the coherent nature of the exciton excitation, which enhances the transition dipole moment throughout the optically active region.[40] Moreover, this effect is boosted by the increased exciton binding energy that results from the strong confinement effect in the 2D perovskite layers. We remark that no enhancement of the nonlinear signal was found in spectral regions other than those of the optical band gaps (refer to the SI section S5 for measurements in the 400−600 nm THG range for the $I_{n=2}$ case).

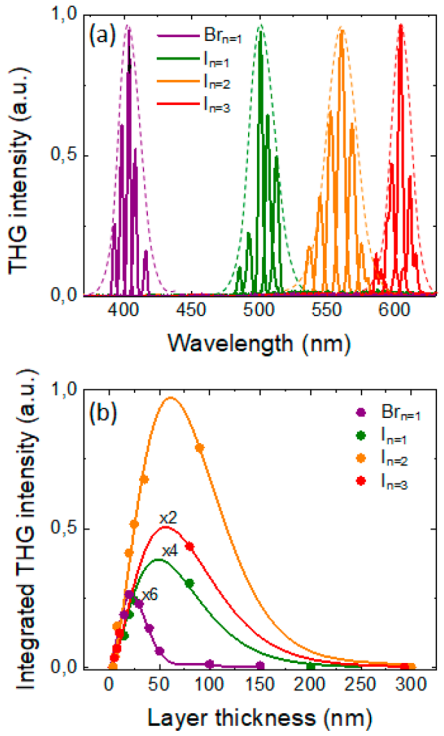

Figure 4. (a) Fundamental wavelength dependence of the THG spectrum for the most efficient flakes of the different perovskite crystals (t = 20 nm for $Br_{n=1}$; t = 80 nm for $I_{n=1}$; t = 90 nm for $I_{n=2}$; t = 80 nm for $I_{n=3}$). Each spectrum corresponds to a different fundamental wavelength, triple that of the central THG wavelength. The envelopes of the sets of spectra, normalized to have equal maximum intensity, are represented with dashed lines. (b) Dependence of the THG signal with the layer thickness for the four different types of crystals excited at resonance. Excitation power used is 1 μW. The solid lines are fits of the experimental data using eq 1.

To gain insight into this resonance feature, we studied the dependence of the THG signal with the flake thickness under resonant excitation for the n = 1 to 3 RPP crystals, as shown in Figure 4b. In all cases, the maximum nonlinear emission is found to occur for intermediate thickness values, as anticipated from the $I_{n=2}$ results shown in Figure 3. To describe this behavior, it is necessary to consider the absorption of the generated THG signal by the emitting material, together with phase-matching conditions between the THG and the fundamental waves, as both of these characteristics introduce thickness-dependent effects. To account for these effects, we utilize the expression for the THG intensity, $I_{3\omega}$, by solving Maxwell's nonlinear equations assuming undepleted excitation for a sufficiently thin material[11]

$$I_{3\omega}(t) = \frac{9\omega^2}{16|\tilde{n}_{3\omega}||\tilde{n}_{\omega}|^3\epsilon_0^2c^4} I_{\omega}^3 |\chi^{(3)}|^2 \left(\frac{e^{-2\alpha t} - 2\cos(\Delta k t)e^{-\alpha t} + 1}{\alpha^2 + \Delta k^2}\right) e^{-2\alpha t} \quad (1)$$

where $\tilde{n}_{\omega}$ and $\tilde{n}_{3\omega}$ are the complex refractive indices at the fundamental and harmonic wavelengths, respectively, $\chi^{(3)}$ is the third order nonlinear susceptibility of the material at the pump wavelength, α is the absorption coefficient at the THG wavelength, and Δk the phase mismatch between the fundamental and harmonic waves. The other parameters in

DOI: 10.1021/acsnano.7b07698
ACS Nano 2018, 12, 644−650

the equation have their usual meaning. Considering that $\tilde{n}_{\omega}$ and $\tilde{n}_{3\omega}$ can be directly obtained from the dielectric function results in Figure 2 $\left(\mathrm{Re}(\tilde{n}) = \sqrt{\frac{|\varepsilon| + \varepsilon_1}{2}};\ \mathrm{Im}(\tilde{n}) = \sqrt{\frac{|\varepsilon| - \varepsilon_1}{2}}\right)$, it is possible to use eq 1 to fit the experimental data in Figure 4b to extract the associated nonlinear susceptibilities. As shown in the figure, notably, a very good quality of the fitting is achieved, as demonstrated by the solid lines in the graph.

Table 1 presents the obtained nonlinear susceptibilities for each perovskite crystal, together with the thickness values

Table 1. $\chi^{(3)}$ and t_{max} Values Obtained from the Fitting of Equation 1 to the Experimental Data in Figure 4b[a]

material	t_{max} (nm)	$\chi^{(3)}$ (10^{-18} m^2/V^2)	fundamental wavelength (nm)	reference
$Br_{n=1}$	22	4.7	1210	this work
$I_{n=1}$	48	3.5	1500	this work
$I_{n=2}$	61	11.2	1675	this work
$I_{n=3}$	56	5.1	1800	this work
BP	14.5	0.14	1557	11
MoS_2	monolayer	0.24	1560	14
graphene	monolayer	0.15	1560	14

[a]Literature values for BP (black phosphorus), MoS_2, and graphene are also included for comparison.

corresponding to the maxima nonlinear signal under resonant excitation, defined here as t_{max}, and reported values for other relevant 2D materials for comparison. It can be noticed that the crystals that present the smallest t_{max} values are $Br_{n=1}$ and $I_{n=1}$, which can be understood from their strong ε_2 at the exciton resonance energies (Figure 2b). At the same time, it is found that the largest nonlinear susceptibilities occur for the samples with the biggest ε_1 at the pump wavelengths (*i.e.*, $I_{n=2}$ and $I_{n=3}$), in agreement with Miller's rule. Remarkably, the $\chi^{(3)}$ values obtained in this work are between one and 2 orders of magnitude larger than those reported for BP, MoS_2, graphene, or 2D perovskite powders.[11,14,43] In particular, since $I_{n=2}$ presents the highest t_{max} and $\chi^{(3)}$ of all samples, it produces the largest THG efficiency.

CONCLUSION

In summary, we have demonstrated that 2D hybrid RPP nanosheets exhibit extremely large third-order optical susceptibilities under resonant exciton excitation, achieving THG conversion efficiencies up to 0.006% for $n = 2$ lead iodide based RPP. The strong third-order optical response is attributed to a large transition dipole moment boosted by the high exciton binding energy of the hybrid organic–inorganic multiple quantum wells. We have also shown that the THG emission intensity varies strongly with the thickness of the perovskite sheets due to signal depletion and phase-matching conditions, and that the optimal thickness lies in the range of 22–61 nm for $n = 1$ to 3 RPP. This work shows the promise of h-BN encapsulated 2D RPP crystals as on-chip optical nonlinear components, paving the way for all optical processing photonic applications.

METHODS

Sample Fabrication. The growth of the different iodide based crystals was performed through a temperature-lowering crystallization method. The process was implemented in an argon-filled glovebox due to the hydroscopic nature of the reactants. For $(BA)_2PbI_4$ ($n = 1$), the following steps were carried out. PbO (Aldrich) and BAI (Dyesol) (1/1 by molar, 0.6 M) were dissolved in a concentrated mixture of HI (Aldrich, 57 wt % in H_2O) and H_3PO_2 (Aldrich, 50 wt % in H_2O) (9:1, v/v) and subsequently heated at 110 °C while stirring to produce a clear yellow solution. The hot solution was then cooled naturally to room temperature, after which orange crystals were obtained. For $(BA)_2MAPb_2I_7$ ($n = 2$), PbO, BAI, and MAI (2/1.4/1 by molar, MAI: 0.3 M) were dissolved in a concentrated mixture of HI and H_3PO_2 (9:1, v/v). The subsequent steps were conducted in a similar way as described above, after which dark red crystals were attained. For $(BA)_2(MA)_2Pb_3I_{10}$ ($n = 3$), PbO, BAI, and MAI (3/1/2 by molar, BAI: 0.2 M) were dissolved in a concentrated mixture of HI (Aldrich, 57 wt % in water) and H_3PO_2 (9:1, v/v). The subsequent steps to obtain the dark brown crystals were carried out in a similar way as described above. Finally, for $(BA)_2PbBr_4$ ($n = 1$), an antisolvent vapor diffusion method was used for crystallizing $(BA)_2PbBr_4$. First, $PbBr_2$ (Aldrich) and BABr (1/2 by molar, $PbBr_2$: 0.5 M) were dissolved in *N*,*N*-dimethylformamide. Subsequently, $(BA)_2PbBr_4$ single crystals were grown by slow diffusion of the vapor of the antisolvent dichloromethane into the solution.

The bulk 2D crystals were mechanically exfoliated onto clean Si/SiO_2 substrates using a scotch-tape method in an argon-filled glovebox. The transferred flakes were then covered with h-BN (<10 nm) *via* the poly(dimethylsiloxane) stamp-transfer method. After the encapsulation of the 2D perovskite flakes with h-BN, the samples were taken out of the glovebox for the nonlinear optical measurements. Atomic force microscopy (see section S8 in the SI for more details) and optical contrast were used to estimate the thickness of the exfoliated flakes.

Optical Characterization. The spectroscopic ellipsometry measurements were carried out on a J.A. Woollam ellipsometer with a wavelength range of 200–2000 nm, tuned using a monochromator. The sample was measured at an incidence angle of 70°. PL measurements were performed using 325 nm ($Br_{n=1}$), 473 nm ($I_{n=1}$), and 532 nm ($I_{n=2,3}$) laser excitation wavelengths. The laser beam was focused on the samples using a 100× objective lens, and the PL signals were collected at a backscattering angle with the same objective lens. The PL emission was routed *via* a bundled optical fiber to a monochromator (Acton, Spectra Pro 2300i) coupled to a CCD (Princeton Instruments, Pixis 400B). For the THG and MPPL characterization, a pulsed Yb:KGW PHAROS laser system was used as the pump of a collinear optical parametric amplifier ORPHEUS with a LYRA wavelength extension option (Light Conversion Ltd., pulse duration of 180 fs, repetition rate of 100 kHz). The excitation beam (λ = 1100–1900 nm) was reflected by a short-pass dichroic mirror (Thorlabs DMSP1000 or Thorlabs DMSP805) and focused onto the sample with a 100× (NA = 0.9) air objective from Nikon (~1 μm^2 spot size). The nonlinear emission was collected in a backscattering configuration *via* the same objective and detected with an avalanche photodiode (MPD PDM Series by Picoquant) for imaging or by a spectrograph (PI Acton SP2300 by Princeton Instruments) for spectral measurements. The sample was fixed to an *XYZ* piezoscanner stage (Nano-Drive, Mad City Laboratories) to perform the scanning. The power of the collected THG emission was measured with a calibrated silicon photodetector (Newport), while the excitation power was characterized with a germanium photodetector (Thorlabs). For <1 pW THG powers, corresponding values were determined from the measured nonlinear spectra.

ASSOCIATED CONTENT

Supporting Information

The Supporting Information is available free of charge on the ACS Publications website at DOI: 10.1021/acsnano.7b07698.

DOI: 10.1021/acsnano.7b07698
ACS Nano 2018, 12, 644–650

Optical images of the millimeter-sized 2D RPP single crystals; powder XRD profiles of the different 2D RPP crystals; exciton binding energy calculation; thickness dependence of photoluminescence (PL) for the 2D RPP flakes; nonlinear optical performance with time; multiphoton absorption photoluminescence; optical images of exfoliated 2D RPP flakes before and after h-BN encapsulation; AFM images of exfoliated 2D RPP flakes (PDF)

AUTHOR INFORMATION

Corresponding Authors

*E-mail: s.maier@imperial.ac.uk.
*E-mail: chmlohkp@nus.edu.sg.

ORCID

Ibrahim Abdelwahab: 0000-0002-0107-5827
Gustavo Grinblat: 0000-0002-1637-9524
Kai Leng: 0000-0003-3408-5033
Yi Li: 0000-0002-6134-3117
Kian Ping Loh: 0000-0002-1491-743X

Author Contributions

I.A. and G.G. contributed equally to this work.

Notes

The authors declare no competing financial interest.

ACKNOWLEDGMENTS

K.P.L. thanks A*Star-DST program 1425203139 "Flexible and high performance perovskite based solar cells on graphene". L.K. thanks Solar Energy Research Institute Singapore (SERIS) for the scholarship support. The authors also acknowledge funding provided by the EPSRC Reactive Plasmonics Programme (EP/M013812/1), the EPSRC Mathematical Fundamentals of Metamaterials Programme (EP/L024926/1), ONR Global, and the Lee-Lucas Chair in Physics. G.G. further acknowledges a Marie Skłodowska-Curie Fellowship.

REFERENCES

(1) Boyd, R. W. *Nonlinear Optics*, 3rd ed.; Academic Press: Burlington, MA, 2008.
(2) Geissbuehler, M.; Bonacina, L.; Shcheslavskiy, V.; Bocchio, N. L.; Geissbuehler, S.; Leutenegger, M.; Marki, I.; Wolf, J. P.; Lasser, T. Nonlinear Correlation Spectroscopy (NLCS). *Nano Lett.* **2012**, *12*, 1668−1672.
(3) Zou, W.; Visser, C.; Maduro, J. A.; Pshenichnikov, M. S.; Hummelen, J. C. Broadband Dye-Sensitized Upconversion of Near-Infrared Light. *Nat. Photonics* **2012**, *6*, 560−564.
(4) Makarov, S. V.; Tsypkin, A. N.; Voytova, T. A.; Milichko, V. A.; Mukhin, I. S.; Yulin, A. V.; Putilin, S. E.; Baranov, M. A.; Krasnok, A. E.; Morozov, I. A.; Belov, P. A. Self-Adjusted All-Dielectric Metasurfaces for Deep Ultraviolet Femtosecond Pulse Generation. *Nanoscale* **2016**, *8*, 17809−17814.
(5) Weigelin, B.; Bakker, G.-J.; Friedl, P. Third Harmonic Generation Microscopy of Cells and Tissue Organization. *J. Cell Sci.* **2016**, *129*, 245−255.
(6) Wang, C.; Cheng, L.; Liu, Z. Drug Delivery with Upconversion Nanoparticles for Multi-Functional Targeted Cancer Cell Imaging and Therapy. *Biomaterials* **2011**, *32*, 1110−1120.
(7) Hong, S. Y.; Dadap, J. I.; Petrone, N.; Yeh, P. C.; Hone, J.; Osgood, R. M. Optical Third-Harmonic Generation in Graphene. *Phys. Rev. X* **2013**, *3*, 021014.
(8) Kumar, N.; Kumar, J.; Gerstenkorn, C.; Wang, R.; Chiu, H.-Y.; Smirl, A. L.; Zhao, H. Third Harmonic Generation in Graphene and Few-Layer Graphite Films. *Phys. Rev. B: Condens. Matter Mater. Phys.* **2013**, *87*, 121406.
(9) Li, Y.; Rao, Y.; Mak, K. F.; You, Y.; Wang, S.; Dean, C. R.; Heinz, T. F. Probing Symmetry Properties of Few-Layer MoS_2 and h-BN by Optical Second-Harmonic Generation. *Nano Lett.* **2013**, *13*, 3329.
(10) Rodrigues, M. J. L. F.; de Matos, C. J. S.; Ho, Y. W.; Peixoto, H.; de Oliveira, R. E. P.; Wu, H. Y.; Neto, A. H. C.; Viana-Gomes, J. Resonantly Increased Optical Frequency Conversion in Atomically Thin Black Phosphorus. *Adv. Mater.* **2016**, *28*, 10693−10700.
(11) Youngblood, N.; Peng, R. M.; Nemilentsau, A.; Low, T.; Li, M. Layer-Tunable Third-Harmonic Generation in Multilayer Black Phosphorus. *ACS Photonics* **2017**, *4*, 8−14.
(12) Malard, L. M.; Alencar, T. V.; Barboza, A. P. M.; Mak, K. F.; de Paula, A. M. Observation of Intense Second Harmonic Generation from MoS_2 Atomic Crystals. *Phys. Rev. B: Condens. Matter Mater. Phys.* **2013**, *87*, 201401.
(13) Yin, X.; Ye, Z.; Chenet, D. A.; Ye, Y.; O'Brien, K.; Hone, J. C.; Zhang, X. ge Nonlinear Optics on a MoS_2 Atomic Monolayer. *Science* **2014**, *344*, 488−490.
(14) Woodward, R.; Murray, R.; Phelan, C.; de Oliveira, R.; Runcorn, T.; Kelleher, E.; Li, S.; de Oliveira, E.; Fechine, G.; Eda, G.; de Matos, C. J. S. Characterization of the Second-and Third-Order Nonlinear Optical Susceptibilities of Monolayer MoS_2 Using Multiphoton Microscopy. *2D Mater.* **2017**, *4*, 011006.
(15) Kim, D. H.; Lim, D. Optical Second-Harmonic Generation in Few-Layer MoS_2. *J. Korean Phys. Soc.* **2015**, *66*, 816−820.
(16) Le, C. T.; Clark, D. J.; Ullah, F.; Senthilkumar, V.; Jang, J. I.; Sim, Y.; Seong, M. J.; Chung, K. H.; Park, H.; Kim, Y. S. Nonlinear Optical Characteristics of Monolayer MoS_2. *Ann. Phys. (Berlin, Ger.)* **2016**, *528*, 551−559.
(17) Janisch, C.; Wang, Y.; Ma, D.; Mehta, N.; Elías, A. L.; Perea-López, N.; Terrones, M.; Crespi, V.; Liu, Z. Extraordinary Second Harmonic Generation in Tungsten Disulfide Monolayers. *Sci. Rep.* **2015**, *4*, 5530.
(18) Ribeiro-Soares, J.; Janisch, C.; Liu, Z.; Elías, A.; Dresselhaus, M.; Terrones, M.; Cançado, L.; Jorio, A. Second Harmonic Generation in WSe_2. *2D Mater.* **2015**, *2*, 045015.
(19) Karvonen, L.; Säynätjoki, A.; Mehravar, S.; Rodriguez, R. D.; Hartmann, S.; Zahn, D. R. T.; Honkanen, S.; Norwood, R. A.; Peyghambarian, N.; Kieu, K.; Lipsanen, H.; Riikonen, J. Investigation of Second- and Third-Harmonic Generation in Few-Layer Gallium Selenide by Multiphoton Microscopy. *Sci. Rep.* **2015**, *5*, 10334.
(20) Deckoff-Jones, S.; Zhang, J.; Petoukhoff, C. E.; Man, M. K. L.; Lei, S.; Vajtai, R.; Ajayan, P. M.; Talbayev, D.; Madéo, J.; Dani, K. M. Observing the Interplay between Surface and Bulk Optical Nonlinearities in Thin Van Der Waals Crystals. *Sci. Rep.* **2016**, *6*, 22620.
(21) Seyler, K. L.; Schaibley, J. R.; Gong, P.; Rivera, P.; Jones, A. M.; Wu, S.; Yan, J.; Mandrus, D. G.; Yao, W.; Xu, X. Electrical Control of Second-Harmonic Generation in a WSe_2 Monolayer Transistor. *Nat. Nanotechnol.* **2015**, *10*, 407.
(22) Trolle, M. L.; Seifert, G.; Pedersen, T. G. Theory of Excitonic Second-Harmonic Generation in Monolayer MoS_2. *Phys. Rev. B: Condens. Matter Mater. Phys.* **2014**, *89*, 235410.
(23) Wang, G.; Marie, X.; Gerber, I.; Amand, T.; Lagarde, D.; Bouet, L.; Vidal, M.; Balocchi, A.; Urbaszek, B. Giant Enhancement of the Optical Second-Harmonic Emission of WSe_2 Monolayers by Laser Excitation at Exciton Resonances. *Phys. Rev. Lett.* **2015**, *114*, 097403.
(24) Agio, M.; Alù, A. *Optical Antennas*; Cambridge University Press: Cambridge, 2013.
(25) Kauranen, M.; Zayats, A. V. Nonlinear Plasmonics. *Nat. Photonics* **2012**, *6*, 737−748.
(26) Grinblat, G.; Li, Y.; Nielsen, M. P.; Oulton, R. F.; Maier, S. A. Efficient Third Harmonic Generation and Nonlinear Subwavelength Imaging at a Higher-Order Anapole Mode in a Single Germanium Nanodisk. *ACS Nano* **2017**, *11*, 953−960.
(27) Cambiasso, J.; Grinblat, G.; Li, Y.; Rakovich, A.; Cortés, E.; Maier, S. A. Bridging the Gap between Dielectric Nanophotonics and the Visible Regime with Effectively Lossless Gallium Phosphide Antennas. *Nano Lett.* **2017**, *17*, 1219−1225.

DOI: 10.1021/acsnano.7b07698
ACS Nano 2018, 12, 644−650

(28) Minovich, A. E.; Miroshnichenko, A. E.; Bykov, A. Y.; Murzina, T. V.; Neshev, D. N.; Kivshar, Y. S. Functional and Nonlinear Optical Metasurfaces. *Laser Photonics Rev.* **2015**, *9*, 195−213.
(29) Yang, Y.; Wang, W.; Boulesbaa, A.; Kravchenko, I. I.; Briggs, D. P.; Puretzky, A.; Geohegan, D.; Valentine, J. Nonlinear Fano-Resonant Dielectric Metasurfaces. *Nano Lett.* **2015**, *15*, 7388−7393.
(30) Li, G.; Zhang, S.; Zentgraf, T. Nonlinear Photonic Metasurfaces. *Nat. Rev. Mater.* **2017**, *2*, 17010.
(31) Capasso, F.; Sirtori, C.; Cho, A. Y. Coupled Quantum Well Semiconductors with Giant Electric Field Tunable Nonlinear Optical Properties in the Infrared. *IEEE J. Quantum Electron.* **1994**, *30*, 1313−1326.
(32) Rosencher, E.; Fiore, A.; Vinter, B.; Berger, V.; Bois, P.; Nagle, J. Quantum Engineering of Optical Nonlinearities. *Science* **1996**, *271*, 168−173.
(33) Cao, D. H.; Stoumpos, C. C.; Farha, O. K.; Hupp, J. T.; Kanatzidis, M. G. 2D Homologous Perovskites as Light-Absorbing Materials for Solar Cell Applications. *J. Am. Chem. Soc.* **2015**, *137*, 7843.
(34) Tsai, H.; Nie, W.; Blancon, J.-C.; Stoumpos, C. C.; Asadpour, R.; Harutyunyan, B.; Neukirch, A. J.; Verduzco, R.; Crochet, J. J.; Tretiak, S.; Pedesseau, L.; Even, J.; Alam, M. A.; Gupta, G.; Lou, J.; Ajayan, P. M.; Bedzyk, M. J.; Kanatzidis, M. G.; Mohite, A. D. High-Efficiency Two-Dimensional Ruddlesden-Popper Perovskite Solar Cells. *Nature* **2016**, *536*, 312−316.
(35) Tan, Z.; Wu, Y.; Hong, H.; Yin, J.; Zhang, J.; Lin, L.; Wang, M.; Sun, X.; Sun, L.; Huang, Y.; et al. Two-Dimensional $(C_4H_9NH_3)_2PbBr_4$ Perovskite Crystals for High-Performance Photodetector. *J. Am. Chem. Soc.* **2016**, *138*, 16612−16615.
(36) Even, J.; Pedesseau, L.; Katan, C. Understanding Quantum Confinement of Charge Carriers in Layered 2D Hybrid Perovskites. *ChemPhysChem* **2014**, *15*, 3733−3741.
(37) Stoumpos, C. C.; Cao, D. H.; Clark, D. J.; Young, J.; Rondinelli, J. M.; Jang, J. I.; Hupp, J. T.; Kanatzidis, M. G. Ruddlesden−Popper Hybrid Lead Iodide Perovskite 2D Homologous Semiconductors. *Chem. Mater.* **2016**, *28*, 2852−2867.
(38) Tanaka, K.; Kondo, T. Bandgap and Exciton Binding Energies in Lead-Iodide-Based Natural Quantum-Well Crystals. *Sci. Technol. Adv. Mater.* **2003**, *4*, 599−604.
(39) Yaffe, O.; Chernikov, A.; Norman, Z. M.; Zhong, Y.; Velauthapillai, A.; van der Zande, A.; Owen, J. S.; Heinz, T. F. Excitons in Ultrathin Organic-Inorganic Perovskite Crystals. *Phys. Rev. B: Condens. Matter Mater. Phys.* **2015**, *92*, 045414.
(40) Hanamura, E.; Nagaosa, N.; Kumagai, M.; Takagahara, T. Quantum Wells with Enhanced Exciton Effects and Optical Non-Linearity. *Mater. Sci. Eng., B* **1988**, *1*, 255−258.
(41) Hanamura, E. Rapid Radiative Decay and Enhanced Optical Nonlinearity of Excitons in a Quantum Well. *Phys. Rev. B: Condens. Matter Mater. Phys.* **1988**, *38*, 1228.
(42) Wu, X.; Trinh, M. T.; Zhu, X.-Y. Excitonic Many-Body Interactions in Two-Dimensional Lead Iodide Perovskite Quantum Wells. *J. Phys. Chem. C* **2015**, *119*, 14714−14721.
(43) Saouma, F. O.; Stoumpos, C. C.; Wong, J.; Kanatzidis, M. G.; Jang, J. I. Selective Enhancement of Optical Nonlinearity in Two-Dimensional Organic-Inorganic Lead Iodide Perovskites. *Nat. Commun.* **2017**, *8*, 742.
(44) Shi, D.; Adinolfi, V.; Comin, R.; Yuan, M.; Alarousu, E.; Buin, A.; Chen, Y.; Hoogland, S.; Rothenberger, A.; Katsiev, K.; Losovyj, Y.; Zhang, X.; Dowben, P. A.; Mohammed, O. F.; Sargent, E. H.; Bakr, O. M. Low Trap-State Density and Long Carrier Diffusion in Organolead Trihalide Perovskite Single Crystals. *Science* **2015**, *347*, 519−522.
(45) Tanaka, K.; Takahashi, T.; Ban, T.; Kondo, T.; Uchida, K.; Miura, N. Comparative Study on the Excitons in Lead-Halide-Based Perovskite-Type Crystals $CH_3NH_3PbBr_3$ $CH_3NH_3PbI_3$. *Solid State Commun.* **2003**, *127*, 619−623.
(46) Tanaka, K.; Takahashi, T.; Kondo, T.; Umeda, K.; Ema, K.; Umebayashi, T.; Asai, K.; Uchida, K.; Miura, N. Electronic and Excitonic Structures of Inorganic−Organic Perovskite-Type Quantum-Well Crystal $(C_4H_9NH_3)_2PbBr_4$. *Jpn. J. Appl. Phys.* **2005**, *44*, 5923.
(47) Dou, L.; Wong, A. B.; Yu, Y.; Lai, M.; Kornienko, N.; Eaton, S. W.; Fu, A.; Bischak, C. G.; Ma, J.; Ding, T. Atomically Thin Two-Dimensional Organic-Inorganic Hybrid Perovskites. *Science* **2015**, *349*, 1518−1521.
(48) Shibanuma, T.; Grinblat, G.; Albella, P.; Maier, S. A. Efficient Third Harmonic Generation from Metal−Dielectric Hybrid Nanoantennas. *Nano Lett.* **2017**, *17*, 2647−2651.

DOI: 10.1021/acsnano.7b07698
ACS Nano 2018, 12, 644−650